

## Evidence of magnetoelectronic electromagnon-mediated transport in flexoelectronic heterostructures

Anand Kataliha <sup>1,\*</sup>, Paul C. Lou,<sup>1,\*</sup> Ravindra G. Bhardwaj <sup>1,\*</sup>, W. P. Beyermann,<sup>2</sup> and Sandeep Kumar <sup>1,3,†</sup>

<sup>1</sup>Department of Mechanical Engineering, University of California, Riverside, California 92521, USA

<sup>2</sup>Department of Physics and Astronomy, University of California, Riverside, California 92521, USA

<sup>3</sup>Materials Science and Engineering Program, University of California, Riverside, California 92521, USA



(Received 13 May 2022; revised 28 February 2023; accepted 27 March 2023; published 11 April 2023)

The superposition of atomic vibrations and flexoelectronic effect gives rise to a cross correlation between free charge carriers and temporal magnetic moment of phonons in conducting heterostructures under an applied strain gradient. The resulting dynamical coupling is expected to give rise to quasiparticle excitations called *magnetoelectronic electromagnons* that carry electronic charge and temporal magnetic moment. Here, we report experimental evidence of magnetoelectronic electromagnons in the freestanding degenerately doped *p*-Si based heterostructure thin film samples. These quasiparticle excitations give rise to long-distance ( $>100\ \mu\text{m}$ ) spin transport, demonstrated using spatially modulated transverse magnetothermoelectric and nonlocal resistance measurements. The magnetoelectronic electromagnons are nonreciprocal and give rise to large magnetochiral anisotropy ( $0.352\ \text{A}^{-1}\ \text{T}^{-1}$ ) that diminishes at lower temperatures. The superposition of nonreciprocal magnetoelectronic electromagnons gives rise to longitudinal and transverse modulations in charge carrier density, spin density, and magnetic moment, demonstrated using the Hall effect and edge dependent magnetoresistance measurements, which can also be called *inhomogeneous magnetoelectronic multiferroic effect*. These quasiparticle excitations are analogous to photons where time dependent polarization and temporal magnetic moment replace electric and magnetic field, respectively, and most likely topological because they manifest topological Nernst effect. Hence, the magnetoelectronic electromagnon can potentially give rise to quantum interference and entanglement effects in conducting solid state systems at room temperature in addition to efficient spin transport.

DOI: [10.1103/PhysRevB.107.165305](https://doi.org/10.1103/PhysRevB.107.165305)

### I. INTRODUCTION

An electromagnon [1–3] is a quasiparticle in a solid state system that can be considered analogous to an electromagnetic wave or photon, where time dependent electric polarization and magnetic moment replace electric and magnetic fields, respectively, as shown in Fig. 1(a). A type of electromagnon, a magnetoactive phonon, can also be considered in the framework of dynamical multiferroicity [4,5], where the superposition of time dependent polarization of phonon ( $\partial_t \mathbf{P}$ ) and ferroelectric polarization ( $\mathbf{P}_{\text{ferroelectric}}$ ) in ferroelectric materials gives rise to temporal magnetic moment [6] ( $\mathbf{M}_t \propto \mathbf{P}_{\text{ferroelectric}} \times \partial_t \mathbf{P}$ ). Recently, an electronic dynamical multiferroicity [7] ( $\mathbf{M}_t \propto \mathbf{P}_{\text{flexoelectronic}} \times \partial_t \mathbf{P}$ ) was experimentally reported in the metal/oxide/degenerately doped Si thin film samples, where flexoelectronic polarization ( $\mathbf{P}_{\text{flexoelectronic}}$ ) replaces the ferroelectric polarization. The electronic dynamical multiferroicity may induce an electromagnonlike excitation in the conducting and nonferroelectric materials. Such a discovery can potentially change the current scientific understanding of the electronic systems with application to quantum computing, spintronics, thermoelectrics, and other future quantum devices.

The flexoelectronic effect is essential for electronic dynamical multiferroicity. In a metal/semiconductor (doped) heterostructure, it can be defined as an electronic response to an applied strain gradient as shown in Figs. 1(b) and 1(c) [8]. The applied strain gradient gives rise to interfacial flexoelectric effect [9], gradient in the band structure [10], and band gap and charge carrier mobility in the bulk of the semiconductor. Tian *et al.* [9], recently, experimentally demonstrated a large piezoelectriclike response in the Si interface under bending loads, which we interpret as interfacial flexoelectric effect in this paper. Similarly, Wang *et al.* [10] reported a large out of plane polarization ( $\approx 0.03\ \text{Cm}^{-2}$ ) in Si due to strain gradient. It, then, triggers a charge carrier injection/extraction from the metal layer to the doped semiconductor layer depending upon the sign (slope) of the strain gradient as shown in Figs. 1(b) and 1(c) [8]. The charge carrier concentration of electrons in a typical metal is of the order of  $10^{22}\ \text{cm}^{-3}$ , whereas the charge carrier concentration in a typical degenerately doped semiconductor is  $10^{19}\ \text{cm}^{-3}$ . Due to flexoelectronic effect, the charge carrier concentration in the semiconductor layer (*p*-Si in the present paper) can rise to the order of  $10^{21}\ \text{cm}^{-3}$ , which is called *flexoelectronic doping* as demonstrated recently [8]. The gradient of excess charge carrier concentration ( $n'$ ) gives rise to a flexoelectronic polarization ( $\mathbf{P}_{\text{flexoelectronic}} \propto n'$ ) in the semiconductor layer as shown in Fig. 1(c) [8]. Such heterostructure samples under applied strain gradient are called *flexoelectronic heterostructures* by us. Hence, the

\*These authors contributed equally to this work.

†Corresponding author: skumar@enr.ucr.edu

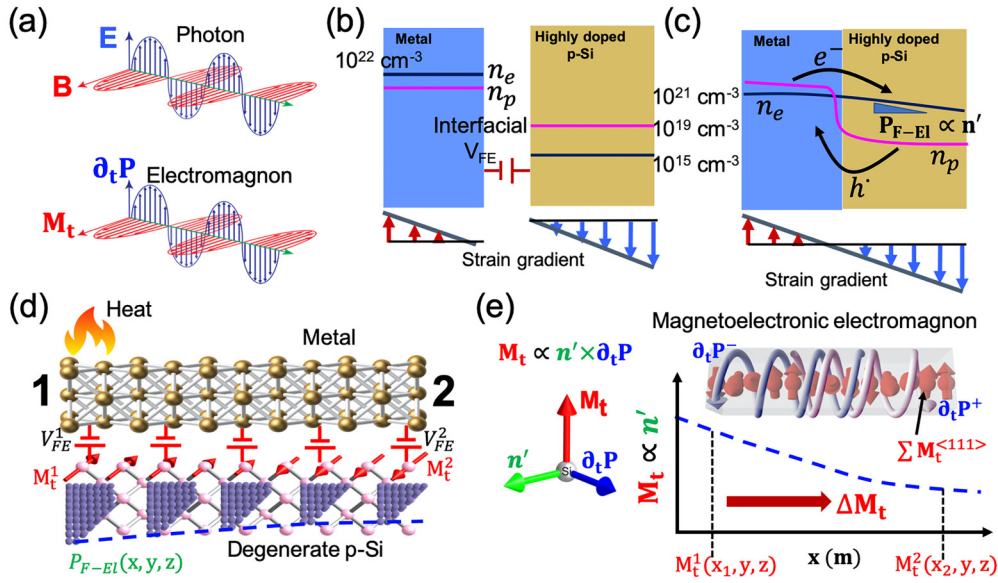


FIG. 1. (a) A schematic showing that electromagnons are analogous to photons. (b) An approximate distribution of charge carrier concentration in a metal/*p*-Si (degenerate) heterostructure. (c) A schematic showing the flexoelectric charge carrier injection in doped Si from the metal layer due to interfacial flexoelectric effect leading to the gradient of the charge carrier in Si and flexoelectric polarization. (d) A schematic showing the perturbation of the flexoelectric charge carrier gradient due to an application of the heat at location 1 and subsequent decay to location 2. (e) A schematic showing the expected longitudinal decay of the flexoelectric charge carrier gradient leading to generation of the magneto-electronic electromagnon that carries electronic charge ( $\Delta n$ ) and magnetic moment ( $\Delta M_t$ ). Also shown is the superposition of magneto-electronic electromagnons' spatial modulations in spin angular momentum.

electromagnon like excitations in metal/doped semiconductor thin film heterostructure samples can be described as

$$M_t^{\pm(hlk)} \propto \mathbf{P}_{\text{flexoelectric}} \times \partial_t \mathbf{P}^{\pm} \propto \mathbf{n}' \times \partial_t \mathbf{P}^{\pm}. \quad (1)$$

We call these excitations in electronic systems *magneto-electronic electromagnons* since they couple to electronic charge as opposed to ionic charge in the case of magneto-electric electromagnons observed in insulating multiferroics. In this paper, we present experimental evidence of nonreciprocal magneto-electronic electromagnons in flexoelectronically doped *p*-Si based heterostructure thin films samples at room temperature. We use spatially modulated magnetothermoelectric and nonlocal resistance measurements to uncover the long-distance spin transport behavior from magneto-electronic electromagnons. The nonreciprocity of magneto-electronic electromagnons is discovered using nonreciprocal transport measurements. Using Hall effect and edge dependent magnetoresistance measurements, we also discover spatial modulations in charge carrier concentration, spin density, and magnetic moment due to the superposition of the topological magneto-electronic electromagnons, which can be considered as inhomogeneous magneto-electronic multiferroic effect.

## II. EXPERIMENTAL RESULTS

Traditionally, electromagnons [1–3] and other quasiparticle excitations are studied using spectroscopic techniques. However, we rely on transport measurements to uncover the evidence of magneto-electronic electromagnons. We hypothesized an experimental scheme having a freestanding Si based flexoelectric heterostructure where strain gradient from residual stresses will give rise to uniform

flexoelectric effect along the length of the sample. However, when the equilibrium state is modified at any given location in the heterostructure [using heat at location 1 as shown in Fig. 1(d)], the interfacial flexoelectric effect ( $V_{\text{flexoelectric}}^1$ ) and consequently flexoelectric polarization of the Si layer will change at this location 1 as shown in Fig. 1(d), whereas the interfacial flexoelectric effect ( $V_{\text{flexoelectric}}^2$ ) and flexoelectric polarization at a distance far away from the heat source remain the same as shown in Fig. 1(d). As a result, the temporal magnetic moment ( $M_t^1$ ) at location 1 will be significantly larger than at location 2 ( $M_t^2$ ) as shown in Figs. 1(d) and 1(e). A longitudinal gradient in the temporal magnetic moment ( $\Delta M_t$ ) will arise across the macroscopic sample in addition to the temperature gradient as shown in Figs. 1(d) and 1(e). A disturbance wave will be generated that will carry the nonequilibrium temporal magnetic moment (or spin angular momentum) along with the heat as shown in Figs. 1(d) and 1(e). As a consequence, magneto-electronic electromagnon excitations will transport electronic charge ( $\Delta n$ ) as well as magnetic moment ( $\Delta M_t$ ) across the macroscopic sample as shown in Figs. 1(d) and 1(e). Therefore, the transport behavior from magneto-electronic electromagnons can be studied using magnetotransport measurements. It is noted that the spin injection from Py to Si layer will be there but it will not be the primary driver of the longitudinal spin chemical potential.

### A. Magnetothermoelectric transport measurement

For the first experimental study, we fabricated a heterostructure composed of Py (25 nm)/MgO (1.8 nm)/SiO<sub>2</sub> (native)/*p*-Si (2  $\mu\text{m}$ ) (sample 1) as shown in Figs. 2(a) and 2(b) (Supplemental Material Sec. S1 [11]). The resistivity

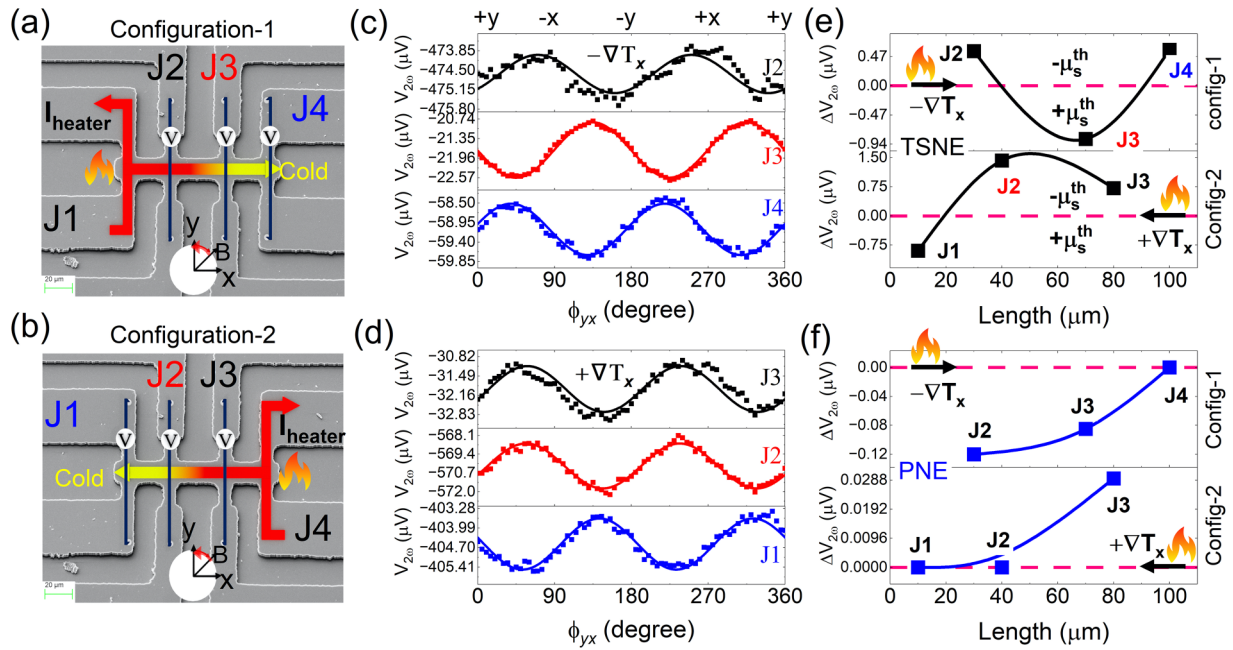


FIG. 2. The scanning electron micrograph showing the representative device structure and experimental scheme for (a) configuration 1 and (b) configuration 2. The angle-dependent transverse magnetothermoelectric response in sample 1 in the  $yx$  plane at a constant applied magnetic field of 1 T (c) measured at  $J2$ ,  $J3$ , and  $J4$  in configuration 1 and (d) measured at  $J3$ ,  $J2$ , and  $J1$  in configuration 2. (e) The longitudinal distribution of the magnitude of transverse spin-Nernst effect for configuration 1 and configuration 2 with possible distribution of spin accumulation. (f) The planar Nernst effect response in control sample 2 showing the longitudinal distribution and response diminishes farther from the heat source. The solid line in panels (e) and (f) is for representation only.

of the Py layer is expected to be  $4.92 \times 10^{-7} \Omega\text{m}$  [8]. The average charge carrier concentration in the  $p$ -Si [7] is expected to increase from  $\approx 4 \times 10^{19} \text{ cm}^{-3}$  ( $2.59 \times 10^{-5} \Omega\text{m}$ ) (multiple control  $p$ -Si samples) to  $\approx 5.45 \times 10^{19} \text{ cm}^{-3}$  ( $1.9 \times 10^{-5} \Omega\text{m}$ ) in case of sample 1. Hence, there is excess charge carrier concentration of  $\approx 1.45 \times 10^{19} \text{ cm}^{-3}$  in sample 1, which leads to flexoelectronic polarization in the  $p$ -Si layer. The MgO layer is used to avoid any interfacial diffusion of the metal layer in the Si layer. The strain gradient in the sample arises due to buckling of the freestanding sample from the residual and processing thermal mismatch stresses including from material deposition [12,13], for which the maximum local strain could be as large as 4% based on previous studies [14]. It is noted that longitudinal inhomogeneities due to inhomogeneous mismatch stresses from geometrical and boundary imperfections may arise. However, these inhomogeneities will average out due to bending and twisting deformation of the freestanding sample. In addition, the free charge carriers will quench any local inhomogeneities in the highly doped Si layer. We measured the angle dependent ( $yx$ -plane) transverse thermoelectric ( $V_{2\omega}$  response) response in sample 1 at 300 K and constant magnetic field of 1 T in two configurations: configuration 1—heat junction  $J1$  using 2 mA and 37 Hz of applied current and measuring response at  $J2$  (30  $\mu\text{m}$ ),  $J3$  (70  $\mu\text{m}$ ), and  $J4$  (100  $\mu\text{m}$ )—and configuration 2—heat junction  $J4$  and measuring response at  $J3$  (30 mm),  $J2$  (70  $\mu\text{m}$ ), and  $J1$  (100  $\mu\text{m}$ ). The measured responses exhibit predominantly a  $\sin 2\phi_{yx}$  angular symmetry (solid line fit) for both configurations as shown in Figs. 2(c) and 2(d) and Supplemental Material Table S1 [11]. The curve fit is found to be better for the responses farther from the heat source as shown in

Figs. 2(c) and 2(d), which can potentially be attributed to larger thermal noise near the heat source. We do not observe  $\sin \phi_{yx}$  symmetry in the angle dependent measurement corresponding to the transverse spin-Seebeck effect [15]. The offset  $V_{2\omega}$  response is attributed to conventional thermopower, which arises due to asymmetries in the overall device structure, which will not be discussed in this paper. The spatial distribution of the angle dependent thermoelectric response is shown in Fig. 2(e) for both configurations. From the spatial distribution of the response, we observe that the responses at junctions  $J3$  and  $J4$  are larger than that at junction  $J2$  in the measurement configuration 1 even though junction  $J2$  is nearer to the heating source as shown in Figs. 2(c) and 2(e) and expected to have larger thermal gradient. Similarly, the angle dependent thermoelectric responses measured at junctions  $J2$  and  $J1$  are larger than response measured at junction  $J3$  even though it is nearer to the heat source in measurement configuration 2 as shown in Figs. 2(d) and 2(e). Such a spatial distribution of the magnetothermoelectric response is not feasible in the diffusive thermal transport regime since thermoelectric response should have decreased exponentially. Instead, the responses at the farthest locations are higher than the nearest locations in both configurations. In addition, the measurements in both configurations show a sign reversal behavior in the measured responses.

The angular symmetry corresponding to  $\sin 2\phi_{yx}$  can arise from the planar Nernst effect  $V_{(\text{PNE})}$  [16] response from the ferromagnetic (Py) layer, which can be described as follows:

$$V_{\text{PNE}} \propto M \times (M \times \nabla T) \quad (2)$$

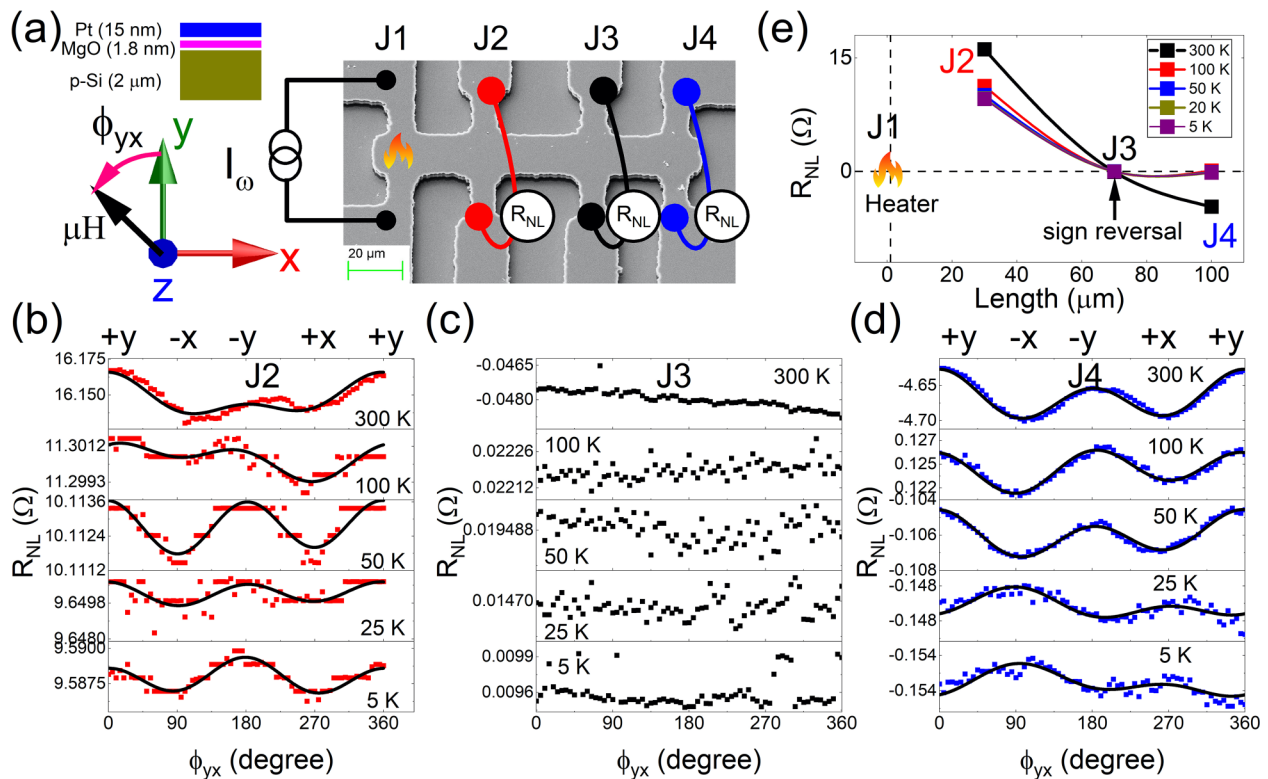


FIG. 3. (a) A representative scanning electron micrograph showing the experimental scheme for angle dependent nonlocal resistance measurement where an alternating current bias is applied across junction  $J1$  and responses are measured simultaneously across junctions  $J2$ ,  $J3$ , and  $J4$ . The angle dependent nonlocal resistance at an applied magnetic field of 4 T in the  $yx$  plane measured at (b)  $J2$ , (c)  $J3$ , and (d)  $J4$  junctions and at 300, 100, 50, 25, and 5 K. The black line represents the curve fit. (e) The spatial distribution of the amplitude of the responses at  $J2$ ,  $J3$ , and  $J4$  showing the sign reversal from potential distribution of temporal magnetic moment and spin accumulation.

where  $M$  and  $\nabla T$  are magnetization vector and temperature gradient, respectively. In this case, the sign of the temperature gradient is constant and the magnetization vector is aligned along the applied magnetic field for any given measurement configuration. Hence, the observed sign reversal cannot arise from the  $V_{\text{PNE}}$  behavior from the ferromagnetic material. Further, the thermal conductivity of 2  $\mu\text{m}$  Si ( $\kappa \approx 80 \text{ W m/k}$ ) [17,18] is expected to be four times larger than that of the Py ( $\kappa \approx 20 \text{ W m/k}$ ) [19] layer. The thermal resistance of the  $p$ -Si layer is expected to be  $\approx 320$  times smaller than that of the Py layer. As a consequence, the heat transport across the Py layer will be negligible as compared to the  $p$ -Si layer in the plane of the sample and out of plane temperature difference will be insignificant. To further support our argument, we measured the angle dependent thermoelectric responses in a control Py/SiO<sub>2</sub> (25 nm)/ $p$ -Si sample (sample 2) as shown in Supplemental Material Fig. S1 and Sec. S2 [11]. The 25-nm SiO<sub>2</sub> intermediate layer extinguishes the spin current as well as the interlayer flexoelectronic charge carrier transfer. In sample 2, the symmetry and sign of the measured responses are the same as expected for  $V_{\text{PNE}}$  behavior as shown in Fig. 2(f), which is consistent with that reported in the previous studies [16]. The  $V_{\text{PNE}}$  response in sample 2 is negative in configuration 1 whereas the response in sample 1 is positive at junction  $J2$  and  $J4$ . Similarly,  $V_{\text{PNE}}$  response in sample 2 is positive in configuration 2 whereas response in sample 1 is negative at junction  $J1$ . The  $V_{\text{PNE}}$  response cannot reverse sign as already stated. Additionally, the  $V_{\text{PNE}}$  response decreases as

expected for diffusive thermal transport as shown in Fig. 2(f). The magnitude of the angle dependent response in sample 2 is orders of magnitude less than that in sample 1. From the symmetry [16], spatial distribution, and magnitude of the angle dependent thermoelectric response, we eliminated  $V_{\text{PNE}}$  as the underlying cause of the observed behavior.

## B. Nonlocal resistance measurement

The flexoelectronic charge carrier transfer from metal to Si layer leaves the metal layer deficient in the charge carrier. As a consequence, there is opposite flexoelectronic effect in the metal layer as well. Hence, the magnetothermoelectric transport could arise in the Py layer itself instead of the  $p$ -Si layer. In order to eliminate current leakage effect [20] and contribution of the Py layer, we did angle dependent nonlocal resistance measurement on a Pt (15 nm)/MgO/ $p$ -Si (2  $\mu\text{m}$ ) sample (sample 3) as a function of temperature where dynamical multiferroicity is already demonstrated [7]. In sample 3, the resistivities of the Pt and  $p$ -Si layers are  $2.52 \times 10^{-7}$  and  $1.1 \times 10^{-5} \Omega\text{m}$  [7], respectively. The expected charge carrier concentration in the  $p$ -Si layer is  $\approx 9.4 \times 10^{19} \text{ cm}^{-3}$  due to flexoelectronic effect [7]. Hence, there is excess charge carrier concentration of  $\approx 5.4 \times 10^{19} \text{ cm}^{-3}$  in sample 3, which leads to flexoelectronic polarization in the  $p$ -Si layer. In this second experiment, we applied 2 mA and 37 Hz of current bias across the junction  $J1$  in a Pt (15 nm)/MgO/ $p$ -Si sample as shown in Fig. 3(a). We, then, measured the angle dependent ( $yx$ -plane)

nonlocal resistance across junctions  $J2$  (30  $\mu\text{m}$ ),  $J3$  (70  $\mu\text{m}$ ), and  $J4$  (100  $\mu\text{m}$ ) for an applied magnetic field of 4 T as shown in Fig. 3(a). The measurement was done at 300, 100, 50, 25, and 5 K. The measurement data for  $J2$ ,  $J3$ , and  $J4$  are shown in Figs. 3(b)–3(d).

The nonlocal resistance can be described using van der Pauw's theorem [20] as

$$R_{\text{NL}} = R_{sq} e^{-\frac{\pi L}{w}} \quad (3)$$

where  $R_{sq} = \frac{\rho}{t}$ ,  $\rho$ ,  $t$ ,  $L$  and  $w$  are resistivity, thickness, length, and width of the channel. Based on the sample dimensions, the nonlocal resistance should be 5 m $\Omega$  at  $J2$  and decrease exponentially along the length, whereas the measured nonlocal resistances are 16.17,  $-0.048$ , and  $-4.6$   $\Omega$  at Hall junctions  $J2$ ,  $J3$ , and  $J4$ , respectively, at 300 K as shown in Figs. 3(b)–3(d). The nonlocal resistance measured at  $J2$  is larger than even the longitudinal resistance (11.38  $\Omega$  between  $J2$  and  $J3$ ) of the sample at 300 K. In another study, the nonlocal resistance measurement on a  $p$ -Si sample is reported to be  $\approx 220$  m $\Omega$  at 30  $\mu\text{m}$  away and  $\approx 32$  m $\Omega$  at 40  $\mu\text{m}$  away from leakage current [21]. Hence, all the responses are orders of magnitude larger than that expected based on leakage current. Further, the response measured at junction  $J4$  is much larger than that at  $J3$  even though  $J4$  is farther away from the current source and nonlocal response should be insignificant according to van der Pauw's theorem. Hence, leakage current can be eliminated as a source of the observed response.

The angle dependent behavior is expected to arise from relationship between magnetic field, flexoelectronic polarization, and temporal magnetic moment. The maximum modulation in the angle dependent response occurs when the magnetic field is aligned either parallel ( $+x$ ) or antiparallel ( $-x$ ) to the direction of transport as shown in Figs. 3(b) and 3(d). Additionally, the magnitudes of the responses are different for parallel and antiparallel configurations as shown in Figs. 3(b) and 3(d). Such a behavior can arise from chiral anomaly [22], which the magnetoelectronic electromagnons are expected to exhibit since they are similar to photons. It is noted that chirality may arise due to twisting deformation of the sample from structural inhomogeneities. We do not observe any angular symmetry in the response measured at junction  $J3$  as shown in Fig. 3(c), which indicates absence of spin polarization. In addition, a sign reversal, similar to magnetothermoelectric response in sample 1, is observed in nonlocal response measured at both  $J3$  and  $J4$  as compared to response at  $J2$  as shown in Fig. 3(e). In the absence of magnetic source, the observed angle dependent nonlocal resistance behavior cannot arise from any other known mechanism. Based on these experiments, the Py and Pt layers are not the underlying cause of magnetothermoelectric and nonlocal resistance responses. These responses are expected to arise due to spin current in the  $p$ -Si layer in both samples 1 and 3.

The magnitude of the nonlocal responses in sample 3 decreases as a function of temperature as shown in Figs. 3(b)–3(e). The sign of the nonlocal responses also changes as the temperature is reduced as shown in Figs. 3(b)–3(e). The conventional nonlocal resistance response cannot change sign as a function of temperature and only a spin dependent

response can change sign. The measurement at  $J4$  shows that the magnitude of the nonlocal resistance (offset response) reduces from 4.6  $\Omega$  at 300 K to  $\approx 0.125$   $\Omega$  at 100 K, which is sharp reduction as shown in Fig. 3(d). In contrast, the nonlocal resistance measured at  $J2$  decreases from 16.17  $\Omega$  at 300 K to 11.3  $\Omega$ . This shows that the Hall junction nearest to the source shows the least reduction as compared to the farthest Hall junction as a function of temperature. The temperature dependent behavior suggests that the phonons are, most likely, the underlying cause of this nonlocal resistance behavior since they freeze at lower temperatures.

We eliminated the  $V_{\text{PNE}}$  and current leakage as an underlying cause of the magnetothermoelectric response observed in sample 1. Hence, the transverse spin Nernst effect  $V_{\text{TSNE}}$  from the nonmagnetic layer ( $p$ -Si in this paper) [23–25] is expected to be the underlying cause of angle dependent magnetothermoelectric response in sample 1, which can be described as

$$V_{\text{TSNE}} \propto M \times (M \times \sigma_s^{\text{th}}) \quad (4)$$

where  $\sigma_s^{\text{th}}$  is the polarization vector of thermal spin accumulation. However, the thermal spin polarization vector in the  $p$ -Si layer has to be spatially modulated along the length of the sample in order to have the observed sign reversal. The electronic thermal transport under spin-orbit coupling (SOC) will give rise to transverse spin current of the same polarity across the length of the sample without any sign reversal. Hence, the sign reversal cannot occur in electronic thermal transport under SOC, which eliminates conventional  $V_{\text{TSNE}}$  response as the underlying cause of the observed behavior.

In contrast, the spatially modulated thermal spin accumulation with opposite polarity can potentially arise from hypothesized magnetoelectronic electromagnon-mediated process due to dynamical multiferroicity. We expect nonreciprocity ( $\partial_t \mathbf{P}^+ \neq \partial_t \mathbf{P}^-$ ) due to lifting of degeneracy from broken structural inversion symmetry. As a consequence, the magnetoelectronic electromagnon with temporal magnetic moment  $M_t^{[1\bar{1}\bar{1}]}$  and  $M_t^{[1\bar{1}1]}$  will not cancel the  $M_t^{[\bar{1}11]}$  and  $M_t^{[\bar{1}\bar{1}1]}$  in the (110) cross-sectional plane [7] of the sample. Hence, the resulting thermal spin accumulation from superposition of the magnetoelectronic electromagnon for the (110) cross-sectional plane can be described as

$$\begin{aligned} \mu_s^{\text{th}}(x, y) &\propto M(x, y) \times \sum M_t^{(hkl)} \\ &= M_t^{[1\bar{1}\bar{1}]} + M_t^{[1\bar{1}1]} + M_t^{[\bar{1}11]} + M_t^{[\bar{1}\bar{1}1]}. \end{aligned} \quad (5)$$

This superposition of the temporal magnetic moments of magnetoelectronic electromagnons, at any location, can give rise to either spin-up or spin-down spin accumulation depending upon their relative contribution as shown in Fig. 1(e). Therefore, the direction of the interlayer spin current as well as measured magnetothermoelectric response will be a function of spatial coordinates having symmetry of  $V_{\text{TSNE}}$  behavior, which is expected to be the underlying cause of sign reversal observed in both the magnetothermoelectric and nonlocal resistance responses. This can also explain absence of any angle dependent response in nonlocal resistance measurement at junction  $J3$  as shown in Fig. 3(c), since the measurements are undertaken over a finite Hall junction width

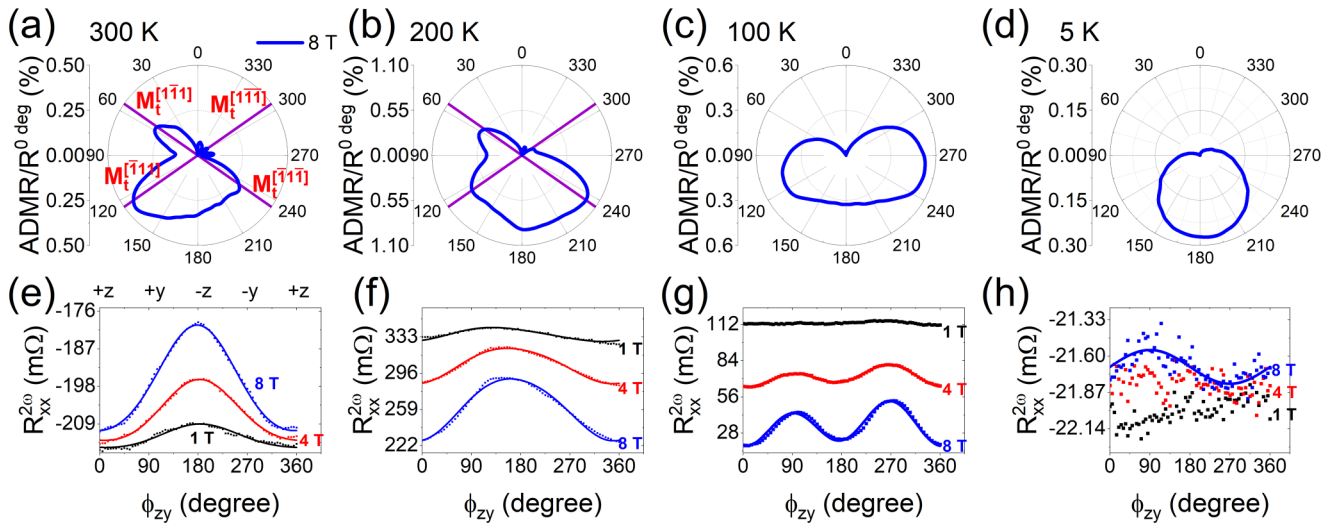


FIG. 4. The angle dependent magnetoresistance behavior in sample 3 for the 8-T magnetic field at (a) 300 K, (b) 200 K, (c) 100 K, and (d) 5 K. The angle dependent second harmonic behavior for applied magnetic field of 1, 4, and 8 T in sample 3 at (e) 300 K, (f) 200 K, (g) 100 K, and (h) 5 K. The solid line represents the curve fit.

and the measured response will be a summation over that finite width, which can be described as

$$\pm\mu_s^{\text{th}}(\text{measured}) = \int \mu_s^{\text{th}}(x, y). \quad (6)$$

The resulting modulations in the local temporal magnetic moment can give rise to a smaller thermal spin accumulation and explain the observed spatial distribution of the measured magnetothermoelectric and nonlocal resistance responses irrespective of the temperature gradient as shown in Figs. 2(e) and 3(e).

### C. Nonreciprocity of the magnetoelectronic electromagnon

To support our mechanistic explanation, a direct evidence of broken structural inversion symmetry and flexoelectronic polarization-mediated nonreciprocity ( $\partial_t P^+ \neq \partial_t P^-$ ) is needed. Hence, we choose to measure the nonreciprocal transport response that arises from the structural inversion asymmetry in sample 3 for the third experiment. In the transport measurements, the resistance of the sample is a function of the direction of the current due to the nonreciprocity. As a consequence, the nonreciprocal resistance can be described as difference:  $\Delta R = R(I) - R(-I)$ . The nonreciprocal resistance can be described in terms of material properties as

$$\Delta R \approx \frac{1}{2}\gamma R_0 I B \quad (7)$$

where  $R_0$ ,  $I$ ,  $B$ , and  $\gamma$  are resistance at zero magnetic field, current, magnetic field, and coefficient of magnetochiral anisotropy [26], respectively. The nonreciprocal transport behavior is studied using longitudinal second harmonic response since it is a quadratic function of applied ac bias as shown in Eq. (7).

Hence, we measured the angle dependent longitudinal resistance and second harmonic resistance for an applied ac bias of 2 mA and 37 Hz and magnetic fields of 1, 4, and 8 T in sample 3 in this third experiment. The sample rotation was carried out in the  $zy$  plane ( $\phi_{zy}$ ) for a constant magnetic

field, which was also the (110) cross-sectional plane. The angle-dependent magnetoresistance (ADMR) measurements exhibit behavior corresponding to dynamical multiferroicity [7] as shown in Figs. 4(a) and 4(b). The magnitude of the ADMR shows peaks corresponding to the  $\langle 111 \rangle$  crystallographic directions [7] (at  $54.7^\circ$  from the  $\pm z$  axis), which disappear at 100 K as shown in Figs. 4(a)–4(d). When the large external magnetic field and, as a consequence, electron spins are aligned parallel to the temporal magnetic moment, the magnetoresistance reduces due to reduced scattering as compared to any other random direction. Hence, the ADMR response will have peaks corresponding to the temporal magnetic moments ( $M_t^{(111)} \propto P_{\text{flexoelectronic}}^{(112)} \times \partial_t P^{(110)}$ ) from dynamical multiferroicity. The ADMR response demonstrates temporal magnetic moments along  $[1\bar{1}1]$ ,  $[\bar{1}11]$ , and  $[\bar{1}\bar{1}\bar{1}]$  crystallographic directions at both 300 and 200 K. The relative magnitudes of the temporal magnetic moments are different at both temperatures. This shows that response along any location and for any given finite length will be a combination of relative contribution of temporal magnetic moments from dynamical multiferroicity as described by Eqs. (5) and (6), which supports our mechanistic explanation for magnetoelectronic electromagnon-mediated spin transport presented earlier. It is noted that the crystallography of the temporal magnetic moment cannot be attributed to the Pt since it is polycrystalline. The dynamical multiferroicity disappears at lower temperatures, which is congruent to the reduction in the nonlocal resistance at junction  $J4$  at 100 K and below in the second experiment on sample 3.

We, then, analyzed the angle dependent longitudinal second harmonic responses at 300, 200, 100, and 5 K, which demonstrate a clear cosine behavior due to nonreciprocal transport behavior at higher temperatures as shown in Figs. 4(e) and 4(f). The measured longitudinal second harmonic response diminished as the temperature was lowered to 100 K as shown in Fig. 4(g). At 5 K, the overall response was negligible and a weak sine behavior was observed at 8 T magnetic field only as shown in Fig. 4(h). Using

the cosine fit, the coefficients of magnetochiral anisotropy are estimated to be 0.151, 0.352, and  $0.071 \text{ A}^{-1} \text{ T}^{-1}$  at 300, 200, and 100 K, respectively. These values are similar to the reported value in Si field-effect transistor (FET) interfaces ( $0.1 \text{ A}^{-1} \text{ T}^{-1}$ ) [26–28] at 2.92 V of gate bias (except Si FET interfaces are two dimensional), while the raw magnitude of the nonreciprocal resistance is similar but the coefficient of magnetochiral anisotropy is smaller than the maximum value of  $1 \text{ A}^{-1} \text{ T}^{-1}$  measured at 2 K reported in BiTeBr [27], which is one of the largest nonreciprocal responses ever reported. However, the magnetochiral anisotropy in BiTeBr [27] drops to a value smaller than that in sample 3 at 200 K. This comparison demonstrates that the magnitude of the flexoelectronic polarization is large. However, a quantitative estimation of the flexoelectronic polarization is not feasible in this paper. The conventional (electronic only processes) nonreciprocal responses increase [27] with reduction in temperature as opposed to the observed behavior in this paper. The observation of dynamical multiferroicity in the ADMR response and large magnetochiral anisotropy in the nonreciprocal response along with their temperature dependent behaviors clearly demonstrate magnetoelectronic electromagnon-mediated (or magnetoactive-phonon-mediated) behavior. The scattering from chiral spin fluctuations as described by Yokouchi *et al.* [29] is expected to be the underlying mechanism, which is expected to arise from the magnetoelectronic electromagnons. The rest of the mechanisms [30] described in the literature are electronic and will not diminish at lower temperatures as stated earlier. Additionally, the observation of magnetochiral anisotropy clearly suggests that the magnetoelectronic electromagnon in flexoelectronically polarized *p*-Si is most likely to be chiral, potentially from twisting deformation. This also supports our previous contention of chiral anomaly in the angle dependent nonlocal resistance response but further studies are needed.

#### D. Spatially modulated electronic property measurement

The magnetothermoelectric and nonlocal resistance measurements showed a longitudinal sign reversal, which we attribute to spatially varying temporal magnetic moment from superposition of the magnetoelectronic electromagnon as described in Eqs. (5) and (6). Since the magnetoelectronic electromagnon arises due to coupling of free charge carrier gradient and phonons, the spatial modulations in charge carrier concentration and magnetic moment must also arise according to Eqs. (1), (5), and (6), which can be observed in Hall and anomalous Hall responses. Further, Eq. (5) describes the superposition of magnetoelectronic electromagnons having opposite temporal magnetic moments and, possibly, chirality. The superposition of two magnetic states with opposite chirality [31] can be described as a spin-density wave (SDW). Hence, the superposition of magnetoelectronic electromagnons is expected to also induce spatial (real space) modulations [32] in the spin density or incommensurate SDW in addition to other electronic properties as stated earlier.

Additionally, we need to establish existence of flexoelectronic effect or charge carrier transfer in the metal-semiconductor heterostructure. Currently, there is no standardized procedure to uncover this phenomenon since

methods used for application of strain gradient inhibit magnetotransport measurements. However, strain state can be modulated using an applied charge current where differential thermal expansion from Joule heating and resulting buckling will modify the strain gradient in a freestanding thin film sample as shown in Fig. 5(a) [8]. The electronic transport measurement as a function of current can be used to indirectly uncover the evidence of flexoelectronic effect. Hence a Hall resistance measurement as a function of space and applied current can be used to present an evidence of both flexoelectronic effect as well as real space modulations from the magnetoelectronic electromagnon.

In the fourth experiment, we measured the Hall resistance response at Hall junctions *J2* and *J3* as a function of applied local current (0.5, 5, and 10 mA at 37 Hz) for an applied magnetic field sweep from 3 to  $-3$  T in sample 1 as shown in Fig. 5(a). In the measurement, the overall transverse responses reduce as a function of applied current as shown in Figs. 5(b) and 5(c). The calculated values of the charge carrier concentrations and the anomalous Hall resistance are listed in Supplemental Material Table S2 [11]. The Hall resistances are negative corresponding to electron as charge carrier. The larger strain gradient at higher current increases the flexoelectronic charge carrier transfer. Assuming the Fermi level to remain the same, the measured average charge carrier concentration is expected to decrease as a function of current due to additional charge carrier transfer from Py to *p*-Si layer. The measured Hall resistances and average charge carrier concentrations indeed reduce as a function of current as shown in Figs. 5(b)–5(e), which proves our hypothesis. This is a direct evidence of the flexoelectronic effect in our sample.

Further analysis shows that the charge carrier concentration is larger at *J2* as compared to *J3* for both positive (spin-up) and negative (spin-down) magnetic fields as shown in Figs. 5(d) and 5(e) at 0.5 mA of applied current. For 5 and 10 mA of applied current, the charge carrier concentration behavior is reversed and the values at *J3* are larger than that at *J2* as shown in Figs. 5(d) and 5(e). The anomalous Hall resistance is larger at *J3* (10.81 m $\Omega$ ) as compared to *J2* (9.77 m $\Omega$ ) for 0.5 mA of current as shown in Fig. 5(f). The anomalous Hall resistance reduces with increased applied current. At 10 mA, the anomalous Hall resistances are similar at both locations [*J2* (6.88 m $\Omega$ ) and *J3* (6.9 m $\Omega$ )]. We estimated a temperature rise of  $\approx 70$  K due to 10 mA of current. Using a control experiment at 375 K as shown in Supplemental Material Sec. S3 and Fig. S2 [11], we eliminate uniform heating as the underlying cause of change in charge carrier concentrations as well as anomalous Hall resistance. The evolution of the anomalous Hall resistance as well as charge carrier concentration as a function of location as well as current is attributed to the spatially modulations in the temporal magnetic moment, charge carrier concentration, and spin-density distribution from magnetoelectronic electromagnons, as hypothesized.

The negative Hall resistance in sample 1 with a 2- $\mu\text{m}$  *p*-Si layer decreases as the current is increased in the previous experiment and any further increase in strain gradient should change the sign of the Hall resistance to positive. A similar behavior is expected to arise in the case of anomalous Hall resistance as well. To induce larger strain gradient, we take a new sample (sample 4) for the fifth experiment

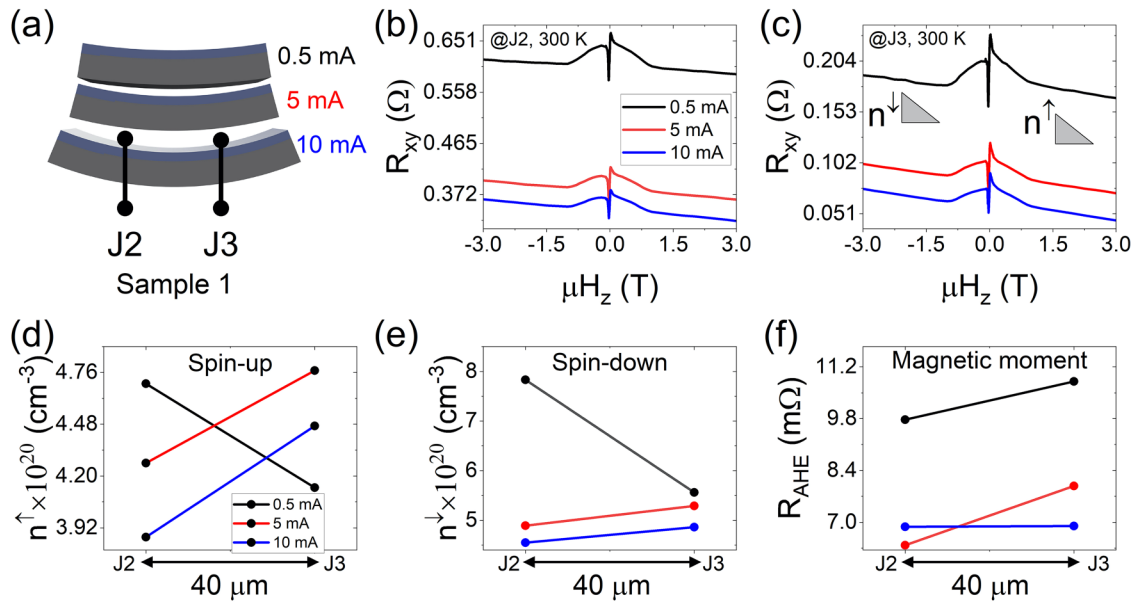


FIG. 5. (a) Schematic showing the increase in strain gradient from buckling of the freestanding sample due to Joule heating from large longitudinal current bias. The Hall response measurement as a function of magnetic field swept from 3 to  $-3$  T at 300 K measured at Hall junction (b)  $J2$  and (c)  $J3$ . (d–f) The spatial modulation of the (d) spin-up charge carrier concentration, (e) spin-down charge carrier concentration, and (f) anomalous Hall resistance as a function of current bias.

where thickness of the  $p$ -Si is reduced by chemical etching [33] to  $\approx 400$  nm while the thickness of the Py layer is kept the same (Supplemental Material Sec. S1 [11]). Due to the thinner  $p$ -Si layer, this new sample will have a significantly larger strain gradient. In the case of sample 4, the  $p$ -Si resistivity at 200 K in the heterostructure needs to be  $6.72 \times 10^{-6} \Omega\text{m}$  as opposed to  $5.45 \times 10^{-5} \Omega\text{m}$  [8]. The charge carrier concentration is expected to increase from  $8.73 \times 10^{18}$  to  $\approx 1.24 \times 10^{21} \text{cm}^{-3}$ , in the case of sample 4, estimated based on a previous report [8], which gives rise to a large flexoelectronic polarization. As expected, we measure the positive Hall resistances at 200 K in this thinner sample for an applied local current of 2 mA and 37 Hz, as shown in Fig. 6(a), as compared to negative in the previous sample (sample 1 with  $2\text{-}\mu\text{m}$   $p$ -Si) due to larger flexoelectronic charge transfer as hypothesized in Fig. 1(c). In addition, the sign of the anomalous Hall resistance also turns negative from

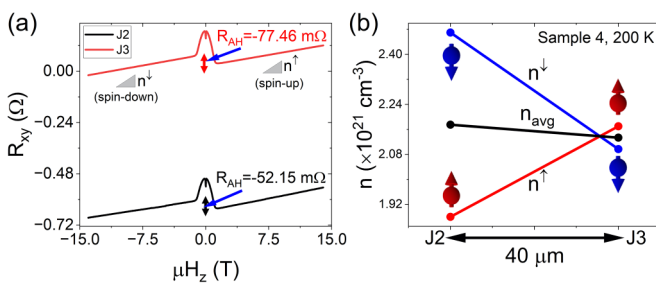


FIG. 6. (a) Hall effect responses at junctions  $J2$  and  $J3$  in a Py (25 nm)/MgO/ $p$ -Si ( $\approx 400$  nm) sample measured at 200 K for an applied magnetic field from 14 to  $-14$  T. (b) The longitudinal modulations in the charge carrier concentration and spin density showing incommensurate SDW-like behavior.

positive. The concentration of the spin-down charge carrier decreases from  $2.47 \times 10^{21} \text{cm}^{-3}$  on the left Hall bar ( $J2$ ) to  $2.09 \times 10^{21} \text{cm}^{-3}$  on the right Hall bar ( $J3$ ) and concentration of spin-up charge carriers increases from  $1.88 \times 10^{21} \text{cm}^{-3}$  on the left to  $2.17 \times 10^{21} \text{cm}^{-3}$  on the right as shown in Fig. 6(b). The average charge carrier concentration decreases from  $2.17 \times 10^{21} \text{cm}^{-3}$  on the left to  $2.13 \times 10^{21} \text{cm}^{-3}$  on the right as shown in Fig. 6(b). Further, the anomalous Hall resistance is significantly smaller at  $J2$  ( $-52.15 \text{ m}\Omega$ ) as compared to  $J3$  ( $-77.46 \text{ m}\Omega$ ) as shown in Fig. 6(a). This reduction in the anomalous Hall resistance can be attributed to the net magnetic moment of opposite magnetoelectronic electromagnons aligning ferromagnetically/antiferromagnetically to the magnetic moment of the Py layer. This reduction can also be attributed to larger local flexoelectronic charge transfer from the Py layer. As compared to sample 1, we observe a crossover between spin-up and spin-down charge carrier concentrations along the length of the sample. The crossover in the spin dependent charge carrier concentration can be attributed to the longitudinal spin-density modulation, which can, potentially, be considered as an incommensurate SDW from the superposition of magnetoelectronic electromagnons [31,34] as described in Eq. (5) and stated earlier. This is a direct evidence of spin density, charge carrier concentrations, and magnetic moment modulations (longitudinal) due to superposition of magnetoelectronic electromagnons. This behavior can also be called *inhomogeneous magnetoelectronic multiferroic effect* since a spatially varying magnetic behavior gives rise to spatially varying electronic properties. This is analogous to the inhomogeneous magnetoelectric effect where spatial magnetic inhomogeneity in a magnetic crystal [35–39] gives rise to electric polarization and vice versa [40].

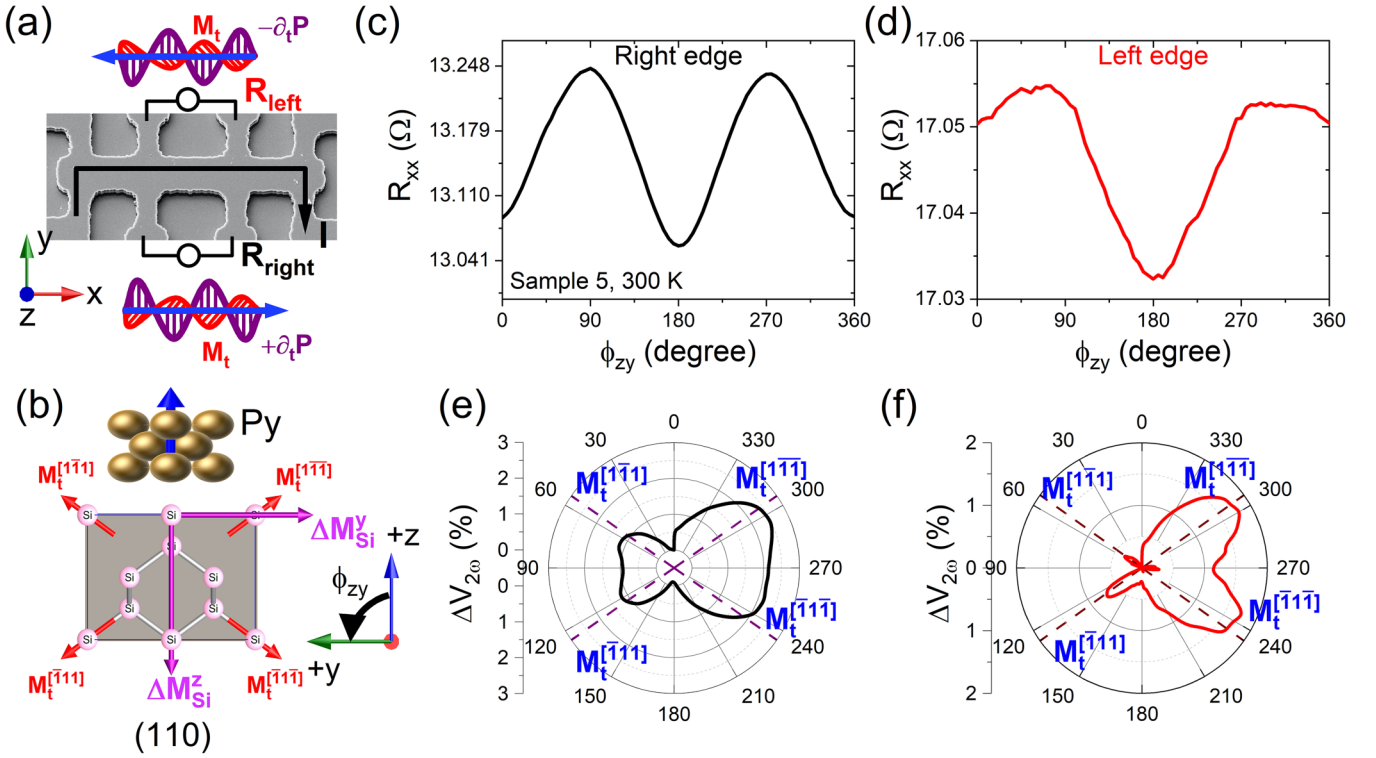


FIG. 7. (a) A representative scanning electron micrograph showing the device structure and experimental scheme. (b) A schematic showing the temporal magnetic moments along  $\langle 111 \rangle$  directions in the  $\langle 110 \rangle$  cross-sectional plane leading to possible  $y$ - and  $z$ -direction net magnetic moments. The angle dependent magnetoresistance in the second Py/MgO/ $p$ -Si sample measured at 300 K for an applied magnetic field of 8 T and angular rotation in the  $zy$ -plane (c) right side and (d) left side of sample 5. The angle dependent longitudinal second harmonic nonreciprocal response measured at 300 K for an applied magnetic field of 8 T and angular rotation in the  $zy$ -plane (e) right side and (f) left side of sample 5.

### E. Edge dependent magnetoresistance measurement

Similar to longitudinal modulations, we expect charge carrier concentration, spin density, and magnetic moment modulation along the width of the samples. To prove it, we measured the angle dependent longitudinal magnetoresistance and nonreciprocal second harmonic responses in a second Py/MgO/ $p$ -Si (2  $\mu\text{m}$ ) sample (sample 5) at two edges for an applied current bias of 2 mA and 37 Hz as shown in Fig. 7(a) in the sixth experiment. The charge carrier concentration in the  $p$ -Si layer is expected to increase to  $\approx 8.7 \times 10^{19} \text{ cm}^{-3}$  in the case of sample 5 as opposed to  $4 \times 10^{19} \text{ cm}^{-3}$ . The measurement shows that the resistance measured at the right edge is  $\approx 23\%$  smaller than that measured at the left edge as shown in Figs. 7(c) and 7(d). Similar behavior is observed in other samples too. The  $R_{\text{left}} = 19.02 \Omega$  and  $R_{\text{right}} = 11.38 \Omega$  are measured at 300 K in sample 3 (with Pt). These are attributed to the transverse charge carrier density modulations as hypothesized.

The ADMR response is composed of anisotropic magnetoresistance (AMR) ( $\sin^2 \theta_{zy}$ ) from the Py layer and two responses having  $\cos \theta_{zy}$  and  $\sin \theta_{zy}$  symmetries (Supplemental Material Sec. S4 [11]). The giant magnetoresistance (GMR) response arises when in-plane current is applied in a thin film heterostructure where two ferromagnets are separated by a nonmagnetic layer. A minimum in magnetoresistance occurs when the magnetic moment in both layers is aligned parallel whereas a maximum occurs when they are antiparallel. In sample 5, the Py layer is one ferromagnet and the

$p$ -Si layer is effectively the second ferromagnet due to net magnetic moment from temporal magnetic moments. Hence, both  $\cos \theta_{zy}$  and  $\sin \theta_{zy}$  responses are attributed to the GMR behavior in sample 5. This measurement shows that a net magnetic moment (potentially canted) having a component in the  $z$  direction ( $\Delta M_{\text{Si}}^z$ ) as well as  $y$  direction ( $\Delta M_{\text{Si}}^y$ ) arises in the flexoelectronically polarized  $p$ -Si thin film as shown in Fig. 7(b). In addition, the net magnetic moments on the left and right edges are significantly different, which gives rise to differences in measurements on the left and right edge, respectively.

As compared to sample 3, where spin dependent scattering from the temporal magnetic moment is observed in magnetoresistance, the second harmonic nonreciprocal responses show peaks corresponding to the temporal magnetic moments along  $\langle 111 \rangle$  directions in the  $\langle 110 \rangle$  cross-sectional plane of the Si thin film layer of sample 5 as shown in Figs. 7(e), 7(f), and 7(b). The response at the right edge corresponds to  $\partial_t \mathbf{P}^{[110]}$  and  $\partial_t \mathbf{P}^{[\bar{1}10]}$  as shown in Fig. 7(e) and can be described as

$$\mathbf{M}^{\text{right}} = \sum \mathbf{M}_t^{\text{right}} = \mathbf{M}_t^{[1\bar{1}\bar{1}]} + \mathbf{M}_t^{[1\bar{1}1]} + \mathbf{M}_t^{[\bar{1}11]} + \mathbf{M}_t^{[\bar{1}\bar{1}1]} \quad (8)$$

whereas the response on the left edge arises primarily from  $\partial_t \mathbf{P}^{[110]}$  as shown in Fig. 7(f) and can be described as

$$\mathbf{M}^{\text{left}} = \sum \mathbf{M}_t^{\text{left}} = \mathbf{M}_t^{[1\bar{1}\bar{1}]} + \mathbf{M}_t^{[\bar{1}11]} + \mathbf{M}_t^{[\bar{1}\bar{1}1]}. \quad (9)$$

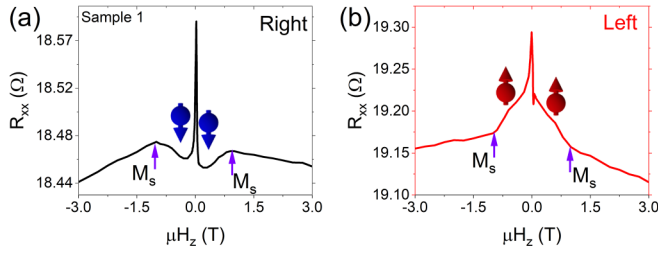


FIG. 8. The edge dependent magnetoresistance measured for an applied magnetic field sweep from 3 to  $-3$  T (a) right edge and (b) left edge in sample 1 at 300 K.

The difference in behavior on two edges is potentially due to spin-Hall effect of the magneto-electronic electromagnon. Hence, a superposition of temporal magnetic moments will give rise to different net magnetic moments (or spin accumulation) along two different edges. It is noted that the temporal magnetic moments are aligned along  $\langle 111 \rangle$  directions that are at  $54.7^\circ$  from the  $\pm z$  axis. As a consequence, the net magnetic moment will be canted from the  $\pm z$  axis, which will give rise to components along the  $z$  axis and  $y$  axis as shown in Fig. 7(b). This is the underlying cause of two GMR responses in the measured ADMR response as hypothesized earlier. Consequently, the out of plane GMR ( $z$  direction,  $\cos\theta_{zy}$ ) response is different between right (0.125%) and left (0.054%) edges as shown in Figs. 7(c) and 7(d), respectively. Similarly, the in-plane GMR ( $y$  direction,  $\sin\theta_{zy}$ ) responses are also estimated to be 0.026 and 0.0028% in the measurement on the right and left edges of the sample, respectively. Additionally, the AMR responses, which arise from the Py layer only, in the sample are also modified due to spin current from the  $p$ -Si layer. The magnitudes of AMR response are estimated to be 1.27 and 0.056% in the measurement on the right and left edges of the sample, respectively.

We also measured the edge dependent magnetoresistance in sample 1 for an applied magnetic field from 3 to  $-3$  T in the seventh experiment as shown in Figs. 8(a) and 8(b). In sample 1,  $R_{\text{left}} = 19.3 \Omega$  and  $R_{\text{right}} = 18.59 \Omega$  are measured at 300 K at zero field. This shows transverse asymmetry similar to other samples. Most importantly, we observe a low field behavior with opposite polarity on opposite edges indicating spin-Hall effect of the magneto-electronic electromagnon. This gives rise to the canted spin state and opposite net magnetic moment from superposition of temporal magnetic moments from the nonreciprocal magneto-electronic electromagnon. This canted spin state arises in the Si layer and is a function of crystallographic orientation of the sample as shown previously [14] since temporal magnetic moment direction will be different along different crystallographic directions. The edge dependent experiments explicitly demonstrate the superposition of the magneto-electronic electromagnons, which is the underlying cause of the spin dependent behavior observed in this paper. Similar to previous studies, the edge dependent experiments demonstrate inhomogeneity in the electronic properties, which is interpreted as inhomogeneous magneto-electronic multiferroic effect.

## F. Topological Nernst effect measurement

The spin transport demonstrated in magnetothermoelectric and nonlocal resistance measurements shows very little dissipation. Further, the edge dependent measurement shows possible evidence of spin-Hall effect of the magneto-electronic electromagnon. Based on these results, we hypothesized that the magneto-electronic electromagnon can potentially be topological. The edge dependent behavior and magnetochiral anisotropy also suggested the same. Hence, we needed an experimental evidence of the topological Berry phase. In the freestanding sample, the longitudinal current leads to self-heating and a heat flow from the center of the sample to the boundaries and electrodes. As a consequence, the second harmonic Hall measurement as a function of out of plane magnetic field is expected to originate from the transverse thermoelectric responses (Nernst effects). We measured the second harmonic Hall response as a function of the out of plane magnetic field from 3 to  $-3$  T at an applied current of 5 mA in sample 1 in the eighth experiment. The measurement at 300 K shows a transverse magnetothermoelectric response attributed to the topological Nernst effect (TNE) [41] as shown in Fig. 9(a). The TNE response is significantly larger than anomalous Nernst effect (ANE) ( $M_z \times \nabla T_x$ ) and ordinary Nernst effect (ONE) ( $B_z \times \nabla T_x$ ) responses, which could not be discerned at 300 K as shown in the Fig. 9(a) inset, whereas the second harmonic Hall response at 20 K is composed of distinct contributions from ONE, ANE, and TNE responses as shown in Fig. 9(b). The TNE response is insignificant at 20 K as compared to 300 K, which is similar to the temperature dependent response observed in nonlocal resistance and nonreciprocal responses in sample 3. This result clearly supports the phononic (magneto-electronic electromagnon) origin of the response from the  $p$ -Si layer since thermal resistance of the  $p$ -Si layer is expected to be  $\approx 320$  times smaller than the Py layer, as stated earlier. This preliminary measurement shows that the magneto-electronic electromagnon is potentially topological, which leads to lack of dissipation observed in magnetothermoelectric and nonlocal resistance measurements. This also explains previously reported large spin-Hall effect in Si [7,14]. This qualitative study only demonstrates observation and trends of TNE response and coefficients are not estimated. Further studies are needed to uncover the origin of the topological Berry phase as well as quantitative estimation of TNE response.

To eliminate the contribution of the Py layer, we, then, measured the Hall resistance and second harmonic Hall response in a MgO (2 nm)/ $p$ -Si (2  $\mu\text{m}$ ) sample (sample 6) at 300 K as a function of magnetic field from 3 to  $-3$  T for an applied current of 1 and 5 mA in the ninth experiment. The Hall resistance and charge carrier concentration do not change when the current is increased from 1 mA ( $3.48 \times 10^{19} \text{ cm}^{-3}$ ) to 5 mA ( $3.47 \times 10^{19} \text{ cm}^{-3}$ ) as shown in Fig. 9(c) unlike the behavior observed in the fourth experiment in sample 1 where the Hall response is a function of current as shown in Figs. 5(b) and 5(c). This presents an explicit proof of flexoelectronic charge carrier transfer in sample 1 and its absence in sample 6. We do not observe any behavior in the second harmonic Hall response at 1 mA of current as shown in Supplemental Material Fig. S4 [11]. However, the second

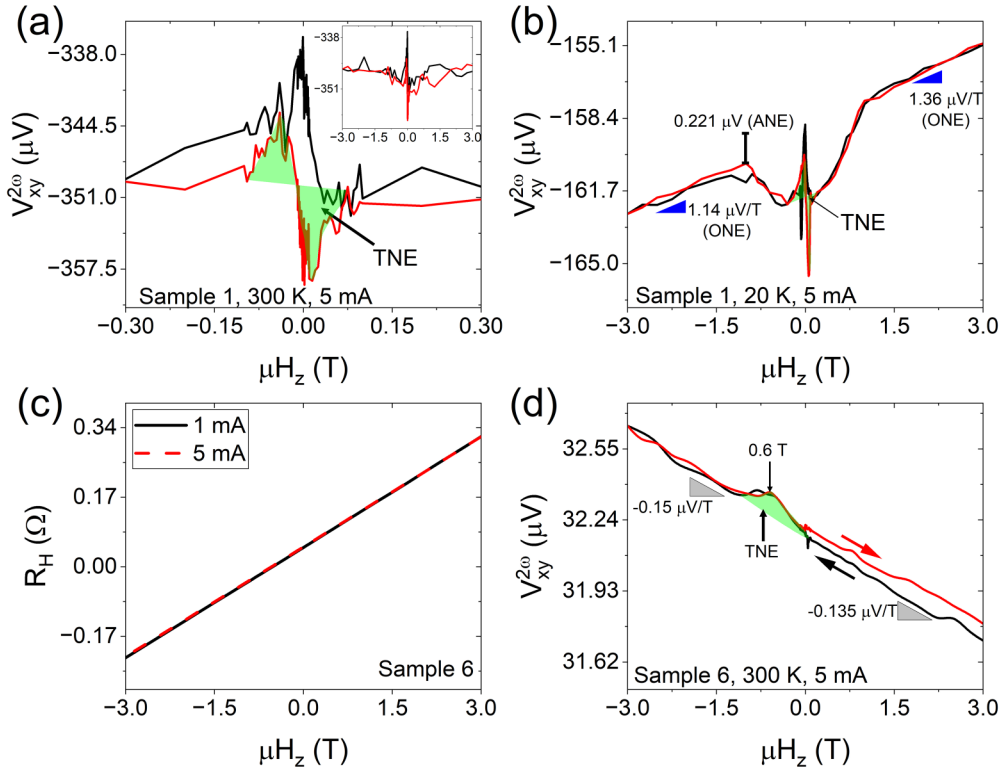


FIG. 9. The second harmonic Hall response as a function of magnetic field from 3 to  $-3$  T for applied current of 5 mA in sample 1 (a) at 300 K and (b) at 20 K. (c) The Hall response measured at 300 K in sample 6 for 1 and 5 mA of applied current bias and a magnetic field sweep between 3 and  $-3$  T. (d) The second harmonic Hall response in sample 6 at 300 K for an applied current bias of 5 mA showing possible TNE behavior. The response in the green shaded region is expected to arise from topological Nernst effect.

harmonic Hall response at 5 mA exhibits a negative slope and the behavior is attributed to the ONE due to the acoustic phonon scattering [42] as shown in Fig. 9(d). Furthermore, the magnitude of the slope is different for negative ( $-0.15 \mu\text{V/T}$ ) and positive ( $-0.135 \mu\text{V/T}$ ) magnetic fields, which indicated potentially a skew scattering behavior, supporting earlier observations. More importantly, a bump at the negative magnetic fields (green shaded region) is observed, as shown in Fig. 9(d). This is a manifestation of the topological Berry phase in thermal transport in the Si layer, leading to TNE [41]. An electromagnetic wave in an inhomogeneous medium experiences a Berry gauge potential in the momentum space, which gives rise to the spin-Hall effect of light [43,44]. Bliokh and Freilikher [45] theoretically demonstrated that transverse acoustic waves in an inhomogeneous medium are analogous to electromagnetic waves. Hence, transverse acoustic waves will also experience phonon spin-orbit coupling due to the Berry gauge potential in the momentum space in a gradient index medium. The strain gradient can be considered equivalent to a gradient index medium in the freestanding thin film structure since a strain field will exist perpendicular to the phonon transport direction. The deflection of a phonon (ray) in an inhomogeneous medium is given by

$$\delta r_{tc} = -\sigma_c \lambda_{r0} \int_C \frac{\mathbf{p}_t \times d\mathbf{p}_t}{p_t^3} = -\sigma_c \lambda_{r0} \frac{\partial \Theta^B}{\partial p_{tc}^{(0)}} \quad (10)$$

where  $\sigma_c$ ,  $\lambda_{r0}$ ,  $\mathbf{p}_t$ , and  $\Theta^B$  are helicity, wavelength, momentum, and Berry phase [45], respectively. As a consequence, the

topological Berry phase is expected to arise in the case of phonon transport in inhomogeneously strained Si thin films. The topological Berry phase of phonons when coupled to flexoelectronic effect gives rise to topological magnetoelectronic electromagnon quasiparticle excitations.

### III. DISCUSSION

Our magnetothermoelectric and nonlocal resistance measurements show a large spin angular momentum transport at macroscopic ( $>100 \mu\text{m}$ ) distance without any significant dissipation, which is the longest such distance ever reported. In case of quantum spin-Hall states [46], quantum-Hall antiferromagnets [47], antiferromagnetic insulators [48–50], magnetic insulators [51], and spin superfluidity [52], the longest distance is an order of magnitude smaller than our measurement, at which spin transport is reported. The thermomagnetic effects, in general, can be described as a cross product of temperature gradient with magnetic moment or magnetic field:  $M \times \nabla T$  and  $B \times \nabla T$ . There is no known thermomagnetic effect that will change sign while the direction of the temperature gradient remains the same. As a consequence, the magnetothermoelectric response and nonlocal resistance behavior cannot arise from thermomagnetic effects. Among all the spin dependent thermomagnetic effects, only the transverse spin-Seebeck effect gives rise to a long-distance spin dependent response as well as sign reversal along the length of the sample [15,53]. The transverse spin-Seebeck effect arises due to the phonon driven spin distribution from the

substrate [54,55]. The transverse spin-Seebeck effect is found to be absent in the suspended Py thin films [16] and our thin film samples are also freestanding. Further, the angle dependent response in sample 1 clearly eliminates transverse spin-Seebeck effect as the underlying reason of spin transport as already stated. The position dependent behavior is also contrary to the expected transverse spin-Seebeck effect response. The nonlocal resistance behavior observed in sample 3 also cannot arise from transverse spin-Seebeck effect since there is no ferromagnetic spin source. Additionally, the experimental observation of dynamical multiferroicity and magnetochiral anisotropy shows that transverse spin-Seebeck effect is not the underlying cause of spin dependent behavior. Based on our experimental study, the superposition of the quasiparticle excitations called the *magneto-electronic electromagnon* from dynamical multiferroicity is the underlying cause of the long-distance spin transport, magnetochiral anisotropy, and spatial modulations in the charge carrier concentrations, spin density, and magnetic moment. The magneto-electronic electromagnons are most likely to be topological quasiparticles. The magneto-electronic electromagnon can also provide a correct microscopic mechanism underlying the previously reported large spin-Hall effect [14], nonlocal transport [21], and magnetothermal transport behavior [18].

#### IV. SUMMARY

In summary, we presented experimental evidence of a quasiparticle excitation called the *magneto-electronic*

*electromagnon* in the degenerately doped *p*-Si based flexoelectronic heterostructures, which carries spin angular momentum and electronic charge. The magneto-electronic electromagnons lead to long-distance spin transport, essential for spintronics applications. The nonreciprocal magneto-electronic electromagnon leads to large magnetochiral anisotropy at room temperature. Additionally, this paper demonstrates superposition of topological magneto-electronic electromagnons that gives rise to spatial modulations in charge carrier density, spin density, and magnetic moment. It is called *inhomogeneous magneto-electronic multiferroic effect*, which can give rise to incommensurate SDW-like behavior. The magneto-electronic electromagnon can also give rise to quantum interference and entanglement from opposite temporal magnetic moments (for example,  $\mathbf{M}_t^{[1\bar{1}1]}$  and  $\mathbf{M}_t^{[\bar{1}11]}$ ) especially at room temperature. Hence, the magneto-electronic electromagnon in flexoelectronic heterostructures can provide an alternate platform for rich and exotic high temperature material behavior that, traditionally, is not expected in conducting electronic systems.

#### ACKNOWLEDGMENTS

The fabrication of experimental devices was completed at the Center for Nanoscale Science and Engineering at University of California, Riverside. Electron microscopy imaging was performed at the Central Facility for Advanced Microscopy and Microanalysis at University of California, Riverside.

The authors declare no competing interests.

- 
- [1] A. Pimenov, A. A. Mukhin, V. Y. Ivanov, V. D. Travkin, A. M. Balbashov, and A. Loidl, *Nat. Phys.* **2**, 97 (2006).
- [2] Y. Takahashi, R. Shimano, Y. Kaneko, H. Murakawa, and Y. Tokura, *Nat. Phys.* **8**, 121 (2012).
- [3] S. Tóth, B. Wehinger, K. Rolfs, T. Birol, U. Stuhr, H. Takatsu, K. Kimura, T. Kimura, H. M. Rønnow, and C. Rüegg, *Nat. Commun.* **7**, 13547 (2016).
- [4] D. M. Juraschek, M. Fechner, A. V. Balatsky, and N. A. Spaldin, *Phys. Rev. Mater.* **1**, 014401 (2017).
- [5] D. M. Juraschek and N. A. Spaldin, *Phys. Rev. Mater.* **3**, 064405 (2019).
- [6] R. M. Geilhufe, V. Juričić, S. Bonetti, J.-X. Zhu, and A. V. Balatsky, *Phys. Rev. Res.* **3**, L022011 (2021).
- [7] P. C. Lou, A. Katailaha, R. G. Bhardwaj, W. P. Beyermann, D. M. Juraschek, and S. Kumar, *Nano Lett.* **21**, 2939 (2021).
- [8] P. C. Lou, A. Katailaha, R. G. Bhardwaj, W. P. Beyermann, D. Mohata, and S. Kumar, *Phys. Rev. B* **105**, 245112 (2022).
- [9] D. Tian, Y. Hou, Q. Pan, and B. Chu, *Phys. Rev. Appl.* **14**, 034008 (2020).
- [10] L. Wang, S. Liu, X. Feng, C. Zhang, L. Zhu, J. Zhai, Y. Qin, and Z. L. Wang, *Nat. Nanotechnol.* **15**, 661 (2020).
- [11] See Supplemental Material at <http://link.aps.org/supplemental/10.1103/PhysRevB.107.165305> for fabrication process, control planar Nernst effect measurement and data, Hall response data, control Hall measurement at 375 K, and control second harmonic Hall data.
- [12] M. Cazzanelli, F. Bianco, E. Borga, G. Pucker, M. Ghulinyan, E. Degoli, E. Luppi, V. Véniard, S. Ossicini, D. Modotto, S. Wabnitz, R. Pierobon, and L. Pavesi, *Nat. Mater.* **11**, 148 (2011).
- [13] C. Schriever, F. Bianco, M. Cazzanelli, M. Ghulinyan, C. Eisenschmidt, J. de Boor, A. Schmid, J. Heitmann, L. Pavesi, and J. Schilling, *Adv. Opt. Mater.* **3**, 129 (2015).
- [14] P. C. Lou, A. Katailaha, R. G. Bhardwaj, T. Bhowmick, W. P. Beyermann, R. K. Lake, and S. Kumar, *Phys. Rev. B* **101**, 094435 (2020).
- [15] K. Uchida, S. Takahashi, K. Harii, J. Ieda, W. Koshibae, K. Ando, S. Maekawa, and E. Saitoh, *Nature (London)* **455**, 778 (2008).
- [16] A. D. Avery, M. R. Pufall, and B. L. Zink, *Phys. Rev. Lett.* **109**, 196602 (2012).
- [17] M. Asheghi, K. Kurabayashi, R. Kasnavi, and K. E. Goodson, *J. Appl. Phys.* **91**, 5079 (2002).
- [18] P. C. Lou, L. de Sousa Oliveira, C. Tang, A. Greaney, and S. Kumar, *Solid State Commun.* **283**, 37 (2018).
- [19] A. D. Avery, S. J. Mason, D. Bassett, D. Wesenberg, and B. L. Zink, *Phys. Rev. B* **92**, 214410 (2015).
- [20] G. Mihajlović, J. E. Pearson, M. A. Garcia, S. D. Bader, and A. Hoffmann, *Phys. Rev. Lett.* **103**, 166601 (2009).
- [21] P. C. Lou and S. Kumar, *J. Phys.: Condens. Matter* **30**, 145801 (2018).

- [22] T. Nomura, X. X. Zhang, S. Zherlitsyn, J. Wosnitza, Y. Tokura, N. Nagaosa, and S. Seki, *Phys. Rev. Lett.* **122**, 145901 (2019).
- [23] D.-J. Kim, C.-Y. Jeon, J.-G. Choi, J. W. Lee, S. Surabhi, J.-R. Jeong, K.-J. Lee, and B.-G. Park, *Nat. Commun.* **8**, 1400 (2017).
- [24] P. Sheng, Y. Sakuraba, Y.-C. Lau, S. Takahashi, S. Mitani, and M. Hayashi, *Sci. Adv.* **3**, e1701503 (2017).
- [25] A. Bose, S. Bhuktare, H. Singh, S. Dutta, V. G. Achanta, and A. A. Tulapurkar, *Appl. Phys. Lett.* **112**, 162401 (2018).
- [26] G. L. J. A. Rikken and P. Wyder, *Phys. Rev. Lett.* **94**, 016601 (2005).
- [27] T. Ideue, K. Hamamoto, S. Koshikawa, M. Ezawa, S. Shimizu, Y. Kaneko, Y. Tokura, N. Nagaosa, and Y. Iwasa, *Nat. Phys.* **13**, 578 (2017).
- [28] D. Choe, M.-J. Jin, S.-I. Kim, H.-J. Choi, J. Jo, I. Oh, J. Park, H. Jin, H. C. Koo, B.-C. Min, S. Hong, H.-W. Lee, S.-H. Baek, and J.-W. Yoo, *Nat. Commun.* **10**, 4510 (2019).
- [29] T. Yokouchi, N. Kanazawa, A. Kikkawa, D. Morikawa, K. Shibata, T. Arima, Y. Taguchi, F. Kagawa, and Y. Tokura, *Nat. Commun.* **8**, 866 (2017).
- [30] Y. Tokura and N. Nagaosa, *Nat. Commun.* **9**, 3740 (2018).
- [31] E. E. Gordon, S. Derakhshan, C. M. Thompson, and M.-H. Whangbo, *Inorg. Chem.* **57**, 9782 (2018).
- [32] Y. Hu, T. Zhang, D. Zhao, C. Chen, S. Ding, W. Yang, X. Wang, C. Li, H. Wang, D. Feng, and T. Zhang, *Nat. Commun.* **13**, 445 (2022).
- [33] P. C. Lou and S. Kumar, *Phys. Status Solidi* **255**, 1700545 (2018).
- [34] J. J. Betouras, G. Giovannetti, and J. van den Brink, *Phys. Rev. Lett.* **98**, 257602 (2007).
- [35] V. G. Bar'yakhtar, V. A. L'vov, and D. A. Yablonskii, *JETP Lett.* **37**, 673 (1983).
- [36] A. P. Pyatakov and A. K. Zvezdin, *Eur. Phys. J. B* **71**, 419 (2009).
- [37] B. M. Tanygin, *J. Magn. Magn. Mater.* **323**, 616 (2011).
- [38] A. K. Zvezdin and A. P. Pyatakov, *Phys. Usp.* **52**, 845 (2009).
- [39] M. Mostovoy, *Phys. Rev. Lett.* **96**, 067601 (2006).
- [40] D. M. Juraschek, Q. N. Meier, M. Trassin, S. E. Trolier-McKinstry, C. L. Degen, and N. A. Spaldin, *Phys. Rev. Lett.* **123**, 127601 (2019).
- [41] X. Li, C. Collignon, L. Xu, H. Zuo, A. Cavanna, U. Gennser, D. Mailly, B. Fauqué, L. Balents, Z. Zhu, and K. Behnia, *Nat. Commun.* **10**, 3021 (2019).
- [42] J. E. Parrott, *Proc. Phys. Soc.* **71**, 82 (1958).
- [43] K. Y. Bliokh, F. J. Rodríguez-Fortuño, F. Nori, and A. V. Zayats, *Nat. Photonics* **9**, 796 (2015).
- [44] K. Y. Bliokh, *J. Opt. A Pure Appl. Opt.* **11**, 094009 (2009).
- [45] K. Y. Bliokh and V. D. Freilikher, *Phys. Rev. B* **74**, 174302 (2006).
- [46] C. Brüne, A. Roth, H. Buhmann, E. M. Hankiewicz, L. W. Molenkamp, J. Maciejko, X.-L. Qi, and S.-C. Zhang, *Nat. Phys.* **8**, 485 (2012).
- [47] P. Stepanov, S. Che, D. Shcherbakov, J. Yang, R. Chen, K. Thilagar, G. Voigt, M. W. Bockrath, D. Smirnov, K. Watanabe, T. Taniguchi, R. K. Lake, Y. Barlas, A. H. MacDonald, and C. N. Lau, *Nat. Phys.* **14**, 907 (2018).
- [48] R. Lebrun, A. Ross, S. A. Bender, A. Qaiumzadeh, L. Baldrati, J. Cramer, A. Brataas, R. A. Duine, and M. Kläui, *Nature (London)* **561**, 222 (2018).
- [49] D. Hou, Z. Qiu, and E. Saitoh, *NPG Asia Mater.* **11**, 35 (2019).
- [50] R. Lebrun, A. Ross, O. Gomonay, V. Baltz, U. Ebels, A. L. Barra, A. Qaiumzadeh, A. Brataas, J. Sinova, and M. Kläui, *Nat. Commun.* **11**, 6332 (2020).
- [51] L. J. Cornelissen, J. Liu, R. A. Duine, J. B. Youssef, and B. J. van Wees, *Nat. Phys.* **11**, 1022 (2015).
- [52] W. Yuan, Q. Zhu, T. Su, Y. Yao, W. Xing, Y. Chen, Y. Ma, X. Lin, J. Shi, R. Shindou, X. C. Xie, and W. Han, *Sci. Adv.* **4**, eaat1098 (2018).
- [53] K. Uchida, J. Xiao, H. Adachi, J. Ohe, S. Takahashi, J. Ieda, T. Ota, Y. Kajiwara, H. Umezawa, H. Kawai, G. E. W. Bauer, S. Maekawa, and E. Saitoh, *Nat. Mater.* **9**, 894 (2010).
- [54] C. M. Jaworski, J. Yang, S. Mack, D. D. Awschalom, J. P. Heremans, and R. C. Myers, *Nat. Mater.* **9**, 898 (2010).
- [55] C. M. Jaworski, J. Yang, S. Mack, D. D. Awschalom, R. C. Myers, and J. P. Heremans, *Phys. Rev. Lett.* **106**, 186601 (2011).